Orbit Maintenance of Quasi-Satellite Trajectories via Mean Relative Orbit Elements

Nicola Baresi, Lamberto Dell'Elce, Josué Cardoso dos Santos, Yasuhiro Kawakatsu

Orbit Maintenance of Quasi-satellite Trajectories via Mean Relative Orbit Elements

Nicola Baresi
ISAS/JAXA, Sagamihara, Japan, 252-5210, nicola.baresi@ac.jaxa.jp

Lamberto Dell'Elce
Université Côte d'Azur & Inria, Sophia Antipolis, France 06902, lamberto.dell-elce@inria.fr

Josué Cardoso dos Santos
São Paulo State University, Guaratingueta, SP, Brazil, 12516-410, josuesantosunesp@gmail.com

Yasuhiro Kawakatsu
ISAS/JAXA, Sagamihara, Japan, 252-5210, yasuhiro.kawakatsu@jaxa.jp

Abstract

The Martian Moons eXploration mission is currently under development at JAXA and will be the first spacecraft mission to retrieve pristine samples from the surface of Phobos. In preparation for the sampling operations, MMX will collect observations of Phobos from stable retrograde relative trajectories also known as quasi-satellite orbits or QSOs. This paper offers a semi-analytical analysis of mid- and high-altitude QSOs in terms of relative orbit elements. Our analysis is not limited to planar orbits and takes into account the eccentricity of the moon's orbit. Furthermore, we introduce a numerical map between mean and osculating orbit elements to study the long-term evolution of MMX and derive a Lyapunov control law for orbit maintenance purposes. The nonlinear controller is based on mean relative orbit element differences and tested with respect to injection errors.

1 Introduction

In order to enhance our comprehension of the Martian system and pave the way for the human exploration of Mars, JAXA is currently planning the Martian Moon eXploration (MMX) mission to Phobos and Deimos [1]. The main goal of MMX is to retrieve pristine samples from the surface of Phobos and return them back to Earth by 2029. Analysis of these samples will be fundamental for understanding the moons' origin and provide valuable information on their composition and geophysical properties [2].

To guarantee the success of the mission as well as the safety of the spacecraft during the sampling operations, months of preparation will follow the arrival of MMX to Mars in 2025. The mission scenario currently envisions early investigations of Phobos from three different quasi-satellite orbits (QSOs) of size 100×200 km, 50×80 km, and 30×50 km in the radial and along-track directions of the planetary satellite, respectively [3]. Ongoing research is also looking at the possibility to further extend these orbits outside the orbital plane of the moon and guarantee

the full coverage of its surface from low altitude QSOs. While this would be a desirable outcome for the scientific return of the mission, it poses new challenges for analytical and semi-analytical methods available in the literature that can only cope with equatorial orbits [4]. Most of these methodologies are also developed in the framework of the circular restricted three-body problem and do not take into account the eccentricity of Phobos' orbit ($e = 0.0151$) [5].

In this research, we introduce a numerical transformation that allows us to map from osculating to mean relative orbit elements (MROE) that better capture the long-term evolution of quasi-satellite orbits in the elliptical Hill problem. This transformation is not restricted to planar orbits and enables the study of three-dimensional QSOs (i.e., with non-zero out-of-plane component). Based on this result, we propose a MROE control strategy that keeps the spacecraft in a desired orbit around Phobos despite insertion errors.

The article is organized as follows. First, we review the equations of the Elliptical Hill Problem (EHP) and present examples of planar quasi-satellite orbits (Section 2). Next, we neglect the gravitational attraction of Phobos and summarize the analytical solution of the unperturbed problem as developed by Yamanaka and Ankersen in [6] (Section 3). In Section 4, we analyze Gauss variational equations and discuss the effects of Phobos' gravity on the relative orbit elements derived from the solution of the unperturbed problem. The results of this investigation are validated in Section 5 by comparison with the numerical integration of the EHP over 100 orbital revolution of Phobos around Mars (i.e., one month circa). In Section 6, we average the linearized equations of motion over one satellite revolution around Phobos and derive the averaged set of equations of motion. These developments are tested with the numerical integration of the averaged systems after the implementation of a mean-to-osculating orbit element mapping that provides reliable initial conditions for bounded relative motion (Section 7). Finally, we apply the analytical and numerical machinery to derive a nonlinear control law that keeps the spacecraft in the neighborhood of a nominal trajectory regardless of its injection errors (Section 8). Conclusions and final remarks are summarized in Section 9.

2 Dynamical Model

Consider the motion of a satellite in the vicinity of Phobos. Both attractors, i.e., Mars and Phobos, are assumed to be spherical and in a Keplerian orbit with eccentricity $e = 0.0151$ and semi-major axis $a = 9377.2\,\mathrm{km}$. It is also assumed that the gravitational attraction excerted by the planetary satellite is much smaller than the tidal force due to Mars. In this case, the equations of motion of the spacecraft are accurately described by the EHP, namely [7, 8]

$$\left\{\begin{array}{rcl} \dot{x} &=& u, \\ \dot{y} &=& v, \\ \dot{z} &=& w, \\ \dot{u} &=& \dfrac{1}{\gamma}\left(g_x + 3\,x\right) + 2\,v, \\ \dot{v} &=& \dfrac{g_y}{\gamma} - 2\,u, \\ \dot{w} &=& \dfrac{g_z}{\gamma} - z, \end{array}\right. \tag{1}$$

where dots denote differentiation with respect to the true anomaly of Phobos around Mars, ν, γ is defined as $1 + e\cos\nu$, and $\boldsymbol{X} = \begin{bmatrix} x, & y, & z, & u, & v, & w \end{bmatrix}^T$ is the state of the satellite (rectangular coordinates) in a pulsating reference frame $\mathcal{S}'$ centered on Phobos and such that $\hat{\boldsymbol{x}}$ is aligned with the separatrix between the two barycenters of the primaries, $\hat{\boldsymbol{z}}$ is parallel to the orbital angular momentum of Phobos, and $\hat{\boldsymbol{y}} = \hat{\boldsymbol{z}} \times \hat{\boldsymbol{x}}$ completes the right-handed triad. The time and

length units are normalized such that one orbital period of Phobos around Mars corresponds to $2\,\pi$, and such that the pulsating *resonance radius* $R = a\,\gamma\,\mu^{(1/3)}$ is equal to 1. The quantity $\mu = 1.6610 \times 10^{-8}$ is the mass ratio between the two primaries, whereas $\begin{bmatrix} g_x, & g_y, & g_z \end{bmatrix}^T$ are the components of Phobos' gravitational attraction as expressed in the synodic reference frame $\mathcal{S}'$.

The System (1) depends explicitly on the independent variable ν. Accordingly, the EHP is a nonautonomous system that does not depend on any parameter as long as the eccentricity of the small body is fixed. Hence, periodic orbits are no longer organized in families, but isolated at best [9]. In particular, the period of a periodic orbit must be resonant with the orbital period of Phobos around Mars.

In actuality, the EHP is better understood and organized by studying families of two-dimensional quasi-periodic invariant tori that replace QSO orbits when $e = 0.0151$.[10] To compute these manifolds, we adapt the numerical algorithm outlined in Gómez & Mondelo [11] and Olikara & Scheeres,[12] and hereby referred to as "GMOS". The main idea of GMOS is that quasi-periodic invariant tori can be calculated via invariant curves of a stroboscopic mapping by solving the boundary value problem described in [13]. The interested reader may find more details on the methodology in the authors' original papers as well as in [14] and [15]. In particular, Olikara[14] provides an exhaustive explanation of the collocation method used in this work to march along the QSO family branch and generate a variety of quasi-periodic invariant tori with $e = 0.0151$. Several examples of quasi-periodic QSO orbits are shown in Fig. 1.

An advantage of the GMOS algorithm is that additional frequencies can be taken into account in order to search for higher-dimensional tori. This feature was demonstrated by Baresi and Scheeres in [16] and is hereby adopted for calculating quasi-periodic QSOs that extend beyond the equatorial plane of Phobos. We refer to this type of orbits as "3D QSOs" and discuss an example of them in Section V.

The purpose of this paper is to study the long-term evolution of three-dimensional QSO trajectories obtained with the GMOS algorithm by means of analytical techniques such as Gauss Variational Equations (GVE) and averaging process. To that end, we begin by neglecting momentarily the gravitational attraction of Phobos and revise the analytical solution of the Keplerian relative motion problem developed by Yamanaka and Ankersen in [6].

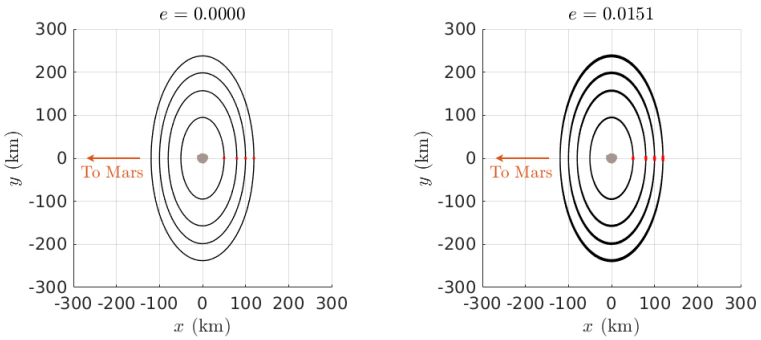

Figure 1: Family members of the QSO (top) and quasi-QSO (bottom) orbit families.

3 The Keplerian Relative Motion Problem

Assuming that the gravitational attraction of Phobos is negligeble, the dynamics of a satellite near the planetary satellite would be governed by the simplified set of equations given by

$$\begin{cases} \dot{x} &= u, \\ \dot{y} &= v, \\ \dot{z} &= w, \\ \dot{u} &= 3\,\dfrac{x}{\gamma} + 2\,v, \\ \dot{v} &= -2\,u, \\ \dot{w} &= -z. \end{cases} \tag{2}$$

The System (2) is equivalent to the equations of the relative motion of two neighboring satellites in eccentric Keplerian orbits and was analytically solved by Yamanaka & Ankersen in [6]. The authors provide an expression for the relative position and velocity vectors in terms of the six integrals of motion K_1, K_2, K_3, K_4, K_5, K_6. The solution reads as

$$\begin{cases} x(\nu) &= K_2\,\gamma\,\sin\nu + K_3\,\gamma\,\cos\nu + K_4\,(2 - 3\,e\,J\,\gamma\,\sin\nu), \\ y(\nu) &= K_1 + K_2\,(1+\gamma)\,\cos\nu \\ & \quad -K_3\,(1+\gamma)\,\sin\nu - 3\,K_4\,J\,\gamma^2, \\ z(\nu) &= K_5\,\sin\nu + K_6\,\cos\nu, \\ u(\nu) &= K_2\,s^* + K_3\,c^* - 3\,e\,K_4\,\left(\dfrac{\sin\nu}{\gamma} + J\,s^*\right), \\ v(\nu) &= -2\,K_2\,\gamma\,\sin\nu - K_3\,(2\,\gamma\,\cos\nu - e) \\ & \quad -3\,K_4\,(1 - 2\,e\,J\,\gamma\,\sin\nu), \\ w(\nu) &= K_5\,\cos\nu - K_6\,\sin\nu, \end{cases} \tag{3}$$

where $s^* = \cos\nu + e\,\cos 2\,\nu$, $c^* = -(\sin\nu + e\,\sin 2\,\nu)$, and J is an integral term defined as $J = \int_{\nu_0}^{\nu} 1/\gamma(\tau)^2\,\mathrm{d}\,\tau$.

Equation (3) can be rewritten in matrix form as

$$\boldsymbol{X}(\nu) = \Phi(\boldsymbol{r}, \boldsymbol{v}, \nu)\,\boldsymbol{K}, \tag{4}$$

with $\boldsymbol{K} = \begin{bmatrix} K_1, & K_2, & K_3, & K_4, & K_5, & K_6 \end{bmatrix}^T$. We note that the determinant of $\Phi(\boldsymbol{r}, \boldsymbol{v}, \nu)$ is equal to $(e^2 - 1)$, so that the matrix is nonsingular for any $e \in [0, 1)$. It follows that the values of $\boldsymbol{K}$ can be inferred from rectangular coordinates through the inverse transformation

$$\boldsymbol{K} = \Phi(\boldsymbol{r}\,\boldsymbol{v}, \nu)^{-1}\,\boldsymbol{X}(\nu). \tag{5}$$

The explicit formulae of $\Phi(\boldsymbol{r}\,\boldsymbol{v}, \nu)^{-1}$ can be found in [17], but do not yield great insight into the geometry of the relative trajectory.

To that end, consider the following auxiliary variables

$$A_x = K_3, \tag{6a}$$

$$A_y = K_2 - 3\,e\,J\,K_4, \tag{6b}$$

$$\delta_x = 2\,K_4, \tag{6c}$$

$$\delta_y = K_1 - 3\,J\,K_4, \tag{6d}$$

$$A = \sqrt{A_x^2 + A_y^2}, \tag{6e}$$

$$\alpha = \arctan\left(\frac{-A_y}{A_x}\right), \tag{6f}$$

$$B = \sqrt{K_5^2 + K_6^2}, \tag{6g}$$

$$\beta = \arctan\left(\frac{K_6}{K_5}\right), \tag{6h}$$

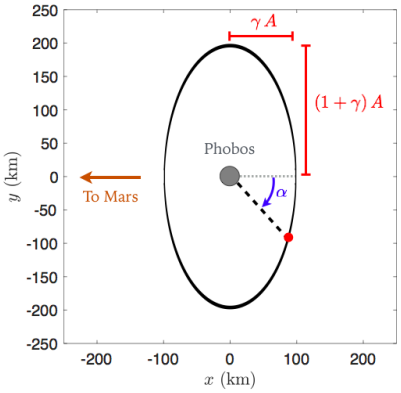

Figure 2: Orbital evolution of a satellite in a 100-km quasi-QSO orbit with $\delta_x = \delta_y = 0$. The red point illustrates the position of the spacecraft at periarion, i.e., when $\nu = 0$.

so that

$$\left\{ \begin{array}{lcl} x(\nu) & = & \gamma\, A\, \cos\left(\nu + \alpha\right) + \delta_x, \\ y(\nu) & = & -(1+\gamma)\, A\, \sin\left(\nu + \alpha\right) + \delta_y, \\ z(\nu) & = & B\, \sin\left(\nu + \beta\right). \end{array} \right. \tag{7}$$

Equation (7) reveals that a mass particle in orbit around a massless Phobos would remain in the vicinity of the Martian moon if A, δ_x, and δ_y have no secular growth. This is guaranteed when $K_4 = 0$ as A_y and δ_y would both remain constant regardless of the integral term appearing in Eq. (6b) and Eq. (6d). If $K_4 = 0$, the trajectory described by the spacecraft in the equatorial plane becomes a pulsating ellipse with frequency $\omega_{xy} = 1$ and semi-major and semi-minor axes equal to $(1+\gamma)\, A$ and $\gamma\, A$, respectively. The phase angles α and β represent the longitude and latitude of the satellite at periarion, i.e., when $\nu = 0$, as specified in Fig. 2). Meanwhile, the out-of-plane motion is decoupled from the planar one and follows an harmonic oscillation with amplitude B and frequency $\omega_z = 1$.

4 Gauss Variational Equations

As specified in Eq. (5), values of $\boldsymbol{K}$ can be inferred from the Cartesian coordinates of a spacecraft while knowing the true anomaly of Phobos around Mars. In consequence, the total differential of $\boldsymbol{K} = \boldsymbol{K}(\boldsymbol{r}, \boldsymbol{v}, \nu)$ reads as

$$\dot{\boldsymbol{K}} = \frac{\partial \boldsymbol{K}}{\partial \boldsymbol{r}}\, \dot{\boldsymbol{r}} + \frac{\partial \boldsymbol{K}}{\partial \boldsymbol{v}}\, \dot{\boldsymbol{v}} + \frac{\partial \boldsymbol{K}}{\partial \nu} \tag{8}$$

and must be equal to zero when the dynamics is governed by the unperturbed case (1), where $\dot{\boldsymbol{v}} = \boldsymbol{a} = \left[3\,\dfrac{x}{\gamma} + 2\,v, \quad -2\,u, \quad -z\right]^T$.

Let us now consider the perturbed System

$$\left\{ \begin{array}{lcl} \dot{\boldsymbol{r}} & = & \boldsymbol{v}, \\ \dot{\boldsymbol{v}} & = & \boldsymbol{a} + \boldsymbol{u}, \end{array} \right. \tag{9}$$

where $\boldsymbol{u} = \left[u_x, \quad u_y, \quad u_z\right]^T$ is a vector of disturbing forces per unit mass in the pulsating synodic reference frame S'. Substituting Eq. (9) in Eq. (8) yields the GVE for the $\boldsymbol{K}$ integrals of motion given by $\dot{\boldsymbol{K}} = \dfrac{\partial \boldsymbol{K}}{\partial \boldsymbol{v}}\, \boldsymbol{u}$.

The rates of change for orbit elements A, α, δ_x, δ_y, B, and β can be now deduced from the application of the chain rule and yields

$$\dot{A} = -\left[\frac{\gamma\,\sin(\nu+\alpha) - 2\,e\,\sin\alpha}{1-e^2}\right] u_x - \left[\frac{e\,\cos\alpha + (1+\gamma)\,\cos(\nu+\alpha)}{1-e^2}\right] u_y + \frac{3\,e\,\sin\alpha}{2\,\gamma^2}\,\delta_x, \tag{10a}$$

$$\dot{\alpha} = -\left[\frac{\gamma\,\cos(\nu+\alpha) - 2\,e\,\cos\alpha}{A\,(1-e^2)}\right] u_x + \left[\frac{e\,\sin\alpha + (1+\gamma)\,\sin(\nu+\alpha)}{A\,(1-e^2)}\right] u_y + \frac{3\,e\,\cos\alpha}{2\,A\,\gamma^2}\,\delta_x, \tag{10b}$$

$$\dot{\delta}_x = \left(\frac{2\,e\,\gamma\,\sin\nu}{1-e^2}\right) u_x + \left(\frac{2\,\gamma^2}{1-e^2}\right) u_y, \tag{10c}$$

$$\dot{\delta}_y = \left[\frac{e\,\gamma\,\cos\nu - 2}{1-e^2}\right] u_x - \left[\frac{e\,(1+\gamma)\,\sin\nu}{1-e^2}\right] u_y - \frac{3}{2\,\gamma^2}\,\delta_x, \tag{10d}$$

$$\dot{B} = \cos(\nu+\beta)\,u_z, \tag{10e}$$

$$\dot{\beta} = -\frac{\sin(\nu+\beta)}{B}\,u_z. \tag{10f}$$

We note that the rate of change of the latitude at periarion is inversely proportional to the magnitude of the out-of-plane motion B. To avoid singularities, we consider

$$\dot{K_5} = (\cos\nu)\,u_z, \tag{11a}$$

$$\dot{K_6} = -(\sin\nu)\,u_z, \tag{11b}$$

instead of Eq. (10e) and Eq. (10f) when studying the dynamical evolution of planar QSO orbits such as the one of Fig. 2.

The final set of equations of motion for the osculating orbit elements $\mathbf{oe} = \begin{bmatrix} A, & \alpha, & \delta_x, & \delta_y, & K_5, & K_6 \end{bmatrix}^T \in \mathcal{M}$ becomes

$$\dot{\mathbf{oe}} = \boldsymbol{F}(\nu, \mathbf{oe}) + G(\nu, \mathbf{oe})\,\boldsymbol{u}. \tag{12}$$

where $\mathcal{M}$ is the phase space of the orbit elements $\mathbf{oe}$,

$$\boldsymbol{F}(\nu, \mathbf{oe}) = \begin{cases} \dfrac{3\,e\,\sin\alpha}{2\,\gamma^2}\,\delta_x, \\ \dfrac{3\,e\,\cos\alpha}{2\,A\,\gamma^2}\,\delta_x, \\ 0, \\ -\dfrac{3}{2\,\gamma^2}\,\delta_x, \\ 0, \\ 0, \end{cases} \tag{13}$$

and $G(\nu, \mathbf{oe})$ is a six-by-three matrix with nonzero components

$$G_{1,1} = -\frac{\gamma\,\sin(\nu+\alpha) - 2\,e\,\sin\alpha}{1-e^2}, \tag{14a}$$

$$G_{1,2} = -\frac{e\,\cos\alpha + (1+\gamma)\,\cos(\nu+\alpha)}{1-e^2}, \tag{14b}$$

$$G_{2,1} = -\frac{\gamma\,\cos(\nu+\alpha) - 2\,e\,\cos\alpha}{A\,(1-e^2)}, \tag{14c}$$

$$G_{2,2} = \frac{e\,\sin\alpha + (1+\gamma)\,\sin(\nu+\alpha)}{A\,(1-e^2)}, \tag{14d}$$

$$G_{3,1} = \frac{2\,e\,\gamma\,\sin\nu}{1-e^2}, \tag{14e}$$

$$G_{3,2} = \frac{2\,\gamma^2}{1-e^2}, \tag{14f}$$

$$G_{4,1} = \frac{e\,\gamma\,\cos\nu - 2}{1-e^2}, \tag{14g}$$

$$G_{4,2} = -\frac{e\,(1+\gamma)\,\sin\nu}{1-e^2}, \tag{14h}$$

$$G_{5,3} = \cos\nu, \tag{14i}$$

$$G_{6,3} = -\sin\nu. \tag{14j}$$

Equation (12) can be now integrated to obtain the evolution of the osculating orbit elements without converting from the Cartesian coordinates adopted in Eq. (9). In addition, analytical expressions for the effects of Phobos' gravity on the osculating orbit elements $\mathbf{oe}$ can be derived and analyzed as in the following Sections.

5 The Effects of Phobos' Gravity

The terms u_x, u_y, u_z appearing in (12) are now replaced with the gravitational attraction of Phobos in the pulsating synodic reference frame $\mathcal{S}'$:

$$\boldsymbol{u} = -\frac{1}{\gamma}\begin{bmatrix} x/r^3 \\ y/r^3 \\ z/r^3 \end{bmatrix}, \tag{15}$$

where $r = \sqrt{x^2+y^2+z^2}$.

Substituting Eq. (7) in r yields a fairly complicated expression for the distance between the satellite and the barycenter of the Martian moon. Nevertheless, a satellite on a QSO orbit remains close to the equatorial plane of Phobos if δ_x and δ_y are close to zero. In addition, the eccentricity of the Martian moon is relatively small and allow for simplifications in the expressions of the GVE presented in Section 3. These considerations justify the first order expansion of the equations of motion in e, $\delta = \left(\frac{\delta_x}{A}\right)$, $\epsilon = \left(\frac{\delta_y}{A}\right)$, $\eta_5 = \left(\frac{K_5}{A}\right)$, $\eta_6 = \left(\frac{K_6}{A}\right)$ under the assumption that $\delta, \epsilon, \eta_5, \eta_6$ $\mathcal{O}(e) << 1$. This assumption was investigated by Cabral in [18] and seems to be reliable for QSO orbits above 80 km based on numerical experiments. In this orbital regime, the expressions of x, y, and z in Eq. (7) imply

$$r(\boldsymbol{e}) \simeq A\sqrt{d^2 + 2\,e\,\cos\nu\,\left[\cos^2\theta + 2\,\sin^2\theta\right] + 2\,\delta\,\cos\theta - 4\,\epsilon\,\sin\theta}, \tag{16}$$

where $\boldsymbol{e} = \begin{bmatrix} e, & \delta, & \epsilon \end{bmatrix}^T$, $d = \sqrt{\cos^2\theta + 4\,\sin^2\theta}$, and $\theta = \nu + \alpha$.

Replacing u_x, u_y, and u_z in Eq. (12) with (15) then yields

$$\begin{aligned}
\dot{A} \simeq & \frac{1}{A^2\,d^3}\,\left\{-\frac{3}{2}\,\sin\left(2\,\theta\right) - 2\,e\,\left[\sin\left(\nu+2\,\alpha\right) - 0.25\,\cos\nu\,\sin\left(2\,\theta\right)\right]\right. \\
& +\delta\,\sin\theta + 2\,\epsilon\,\cos\theta \\
& \left. +\frac{9}{2}\,\sin\left(2\,\theta\right)\,\left[\frac{e\,\cos\nu\,\left(\cos^2\theta+2\,\sin^2\theta\right)+\delta\,\cos\theta-2\,\epsilon\,\sin\theta}{d^2}\right]\right\}, \qquad (17a) \\
\dot{\alpha} \simeq & \frac{1}{A^3}\,\left\{\frac{1}{d} - e\,\frac{\cos\nu}{d}\right. \\
& -\frac{e\,\left[2\,\cos\left(\nu+2\,\alpha\right)+\cos\nu\,\left(\cos^2\theta+2\,\sin^2\theta\right)\right]}{d^3} \\
& \left. -\frac{2\,\delta\,\cos\theta-4\,\epsilon\,\sin\theta}{d^3}\right\}, \qquad (17b) \\
\dot{\delta}_x \simeq & \frac{2\,A}{[r(\boldsymbol{e})]^3}\,\left\{2\,\sin\theta + e\,\left[3\,\cos\nu\,\sin\theta-\sin\nu\,\cos\theta\right]-\epsilon\right\}, \\
\simeq & \frac{2}{A^2}\,\left\{\left[\frac{2\,\sin\theta+e\,\left[3\,\cos\nu\,\sin\theta-\sin\nu\,\cos\theta\right]-\epsilon}{d^3}\right]\right. \\
& \left. -6\,\sin\theta\,\left[\frac{e\,\cos\nu\,\left[\cos^2\theta+2\,\sin^2\theta\right]+\delta\,\cos\theta-2\,\epsilon\,\sin\theta}{d^5}\right]\right\}. \qquad (17c) \\
\dot{\delta}_y \simeq & \frac{1}{A^2\,d^3}\,\left\{2\,\cos\theta - e\,\left[\cos\nu\,\cos\theta+4\,\sin\nu\,\sin\theta\right]+\delta\,\left(\frac{4-3\,A^3\,d^3}{2}\right)\right. \\
& \left. -6\,\cos\theta\,\left[\frac{e\,\cos\nu\,\left(\cos^2\theta+2\,\sin^2\theta\right)+\delta\,\cos\theta-2\,\epsilon\,\sin\theta}{d^2}\right]\right\}, \qquad (17d) \\
\dot{K}_5 \simeq & -\frac{\cos\nu}{A^2}\,\left(\frac{\eta_5\,\sin\nu+\eta_6\,\cos\nu}{d^3}\right), \qquad (17e) \\
\dot{K}_6 \simeq & \frac{\sin\nu}{A^2}\,\left(\frac{\eta_5\,\sin\nu+\eta_6\,\cos\nu}{d^3}\right), \qquad (17f)
\end{aligned}$$

or

$$\dot{\boldsymbol{oe}} = \boldsymbol{g}(\nu, \boldsymbol{oe}) \qquad (18)$$

in vectorial form.

Equation (18) introduces a Linear Model (LM) in e, δ, ϵ, η_5, and η_6 that accurately predicts the dynamics of mass particles in mid- and high-altitude QSO orbits for several orbital periods around Phobos. This claim is supported by Fig. 3–5, which compare trajectories of the original and linearized systems obtained by numerical integration of the same set of initial conditions:

$$\boldsymbol{x}(\nu_0) = \begin{bmatrix} 4.223784177246 \\ -0.0814069532286406 \\ -0.317146285024353 \\ 0.0342016222056316 \\ -8.42418511932641 \\ 0.139224827215046 \end{bmatrix}, \qquad (19a)$$

$$\boldsymbol{oe}(\nu_0) = \begin{bmatrix} 4.22922122381657 \\ 0.61341331263205 \\ -0.0576706532250935 \\ -0.0778356681681636 \\ 0.296336249720383 \\ -0.179304617116979 \end{bmatrix}, \qquad (19b)$$

in Cartesian coordinates and osculating orbit elements, respectively, with $\nu_0 = 324.8780$ deg.

As depicted in Fig. 5(a), the error between the integration of Eq. (12) and Eq. (9) is purely numerical and negligible after 100 orbital revolutions of Phobos around Mars (i.e., almost 32 days). In contrast, the position error of the linearized model exhibits a secular growth, but never exceeds 5 kilometers over the same interval of time. Such an error is deemed reasonable for the purpose of this article, as navigation errors and mismodeled dynamics would likely overtake the inaccuracies of the linearized model over the time span of a few days. In this time frame, the LM is considered as a good candidate for describing the long-term evolution of satellites in QSO orbits and can be used for the analysis of the secular motion as described in the following Section.

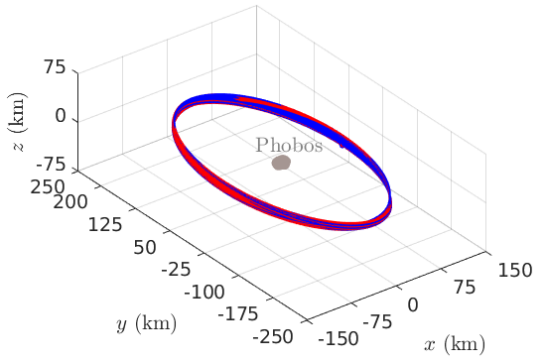

Figure 3: Quasi-QSO orbit integrated over 100 Phobos revolution with the LM (blue) and GVEs (red) models.

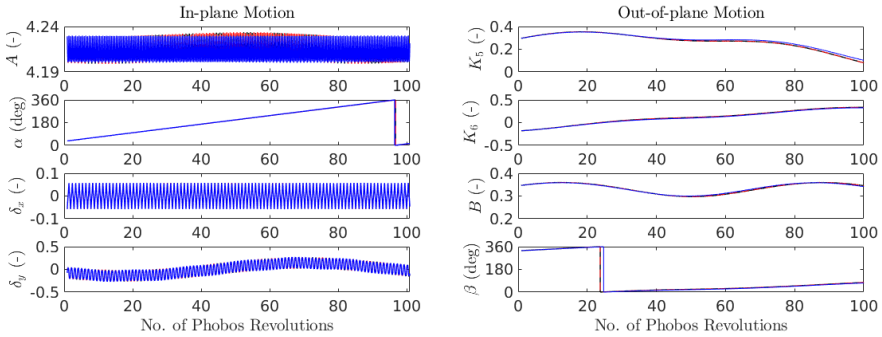

(a) (b)

Figure 4: top) A, α, δ_x, δ_y obtained with the LM (blue) and GVEs (red) models. bottom) K_5, K_6, B, β obtained with the LM (blue) and GVEs (red) models.

6 Averaged Equations

The long-term evolution of quasi-QSO orbits is now analyzed by averaging Eq. (17) over one orbital period around Phobos, i.e., $\dot{\bar{\mathbf{oe}}} = \int_0^{2\pi} \dot{\mathbf{oe}}\, \mathrm{d}\theta$. We find that the averaged orbit elements $\bar{A}$,

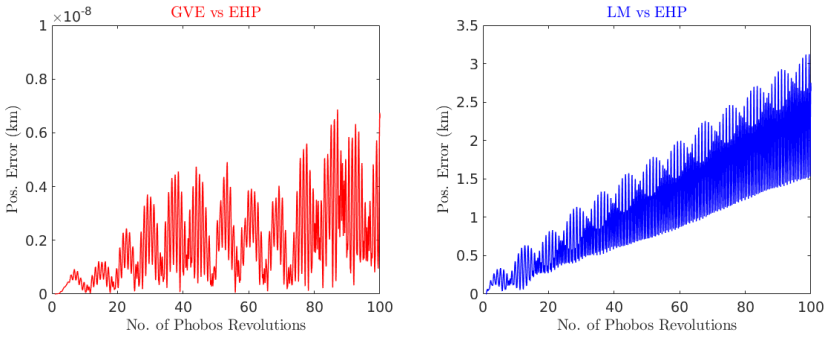

(a) (b)

Figure 5: (a) Position error between the GVEs and EHP models. (b) Position error between the LM and EHP models.

$\bar{\alpha}$, $\bar{\delta}_x$, $\bar{\delta}_y$, $\bar{K}_5$, and $\bar{K}_6$ evolve with the true anomaly as according to

$$\dot{\bar{A}} = 0, \tag{20a}$$

$$\dot{\bar{\alpha}} = \frac{\mathcal{K}}{\pi\,\bar{A}^3}, \tag{20b}$$

$$\dot{\bar{\delta}}_x = -2\,\frac{e}{\bar{A}^2}\left(\frac{\mathcal{K}-7\,\mathcal{E}}{9\,\pi}\right)\sin\bar{\alpha} + 2\,\frac{\bar{\delta}_y}{\bar{A}^3}\left(\frac{\mathcal{K}-\mathcal{E}}{3\,\pi}\right), \tag{20c}$$

$$\dot{\bar{\delta}}_y = \frac{e}{\bar{A}^2}\left(\frac{\mathcal{K}-52\,\mathcal{E}}{9\,\pi}\right)\cos\bar{\alpha} - \frac{3}{2}\,\bar{\delta}_x + 2\,\frac{\bar{\delta}_x}{\bar{A}^3}\left(\frac{\mathcal{K}-4\,\mathcal{E}}{3\,\pi}\right), \tag{20d}$$

$$\dot{\bar{K}}_5 = -\frac{\bar{K}_5}{\bar{A}^3}\left(\frac{2\,\mathcal{K}-5\,\mathcal{E}}{6\,\pi}\right)\sin(2\,\bar{\alpha}) - \frac{\bar{K}_6}{\bar{A}^3}\,\frac{\mathcal{E}}{2\,\pi} + \frac{\bar{K}_6}{\bar{A}^3}\left(\frac{2\,\mathcal{K}-5\,\mathcal{E}}{6\,\pi}\right)\cos(2\,\bar{\alpha}), \tag{20e}$$

$$\dot{\bar{K}}_6 = \frac{\bar{K}_5}{\bar{A}^3}\,\frac{\mathcal{E}}{2\,\pi} + \frac{\bar{K}_5}{\bar{A}^3}\left(\frac{2\,\mathcal{K}-5\,\mathcal{E}}{6\,\pi}\right)\cos(2\,\bar{\alpha}) + \frac{\bar{K}_6}{\bar{A}^3}\left(\frac{2\,\mathcal{K}-5\,\mathcal{E}}{6\,\pi}\right)\sin(2\,\bar{\alpha}), \tag{20f}$$

where $\mathcal{K} \simeq 2.156516$ and $\mathcal{E} \simeq 1.211056$ are the complete elliptic integrals of the first and second kind, respectively, evaluated with modulus $k = \sqrt{3}/2$ [19].

We note that our expressions are different from the ones of Cabral [18] and are rather similar to the ones of Kogan [5] whenever $e \to 0$. Indeed, as emphasized in [5], Eq. (20) exhibits cross-coupling between some of the orbit elements, as well as long-term oscillations due to the secular growth of α, i.e., the longitude at periarion. The secular growth of α causes the geometrical configuration between the spacecraft, Mars, and Phobos, to change at every periarion passage, i.e., when the gravitational attraction of Mars is at its strongest. To grasp the secular effects of this phenomenon, note that $\bar{\alpha}$ grows linearly with the true anomaly and with a rate that depends on the amplitude of the in-plane motion via

$$\bar{\alpha}(\nu) = \omega_\alpha\,(\nu - \nu_0) + \bar{\alpha}_0, \tag{21}$$

where $\omega_\alpha = (\mathcal{K}/\pi)\,\bar{A}^{-3} \simeq 0.686440\,\bar{A}^{-3}$, $\bar{\alpha}_0 = \bar{\alpha}(\nu_0)$, and ν_0 is the true anomaly of Phobos at epoch.

Observe that ω_α is constant due to Eq. (20a). Furthermore, the value of ω_α defines the period of the QSO orbit around Phobos as $T = 2\,\pi/n_{QSO}$, and $n_{QSO} = \dot{\theta} = \dot{\nu} + \dot{\alpha} \simeq 1 + \omega_\alpha$. This is demonstrated with the chart of Fig. 6, illustrating the comparison between the analytical prediction of n_{QSO} and the numerical value computed with the GMOS algorithm of Section II. We find that the proposed linearization and averaging approach is only valid when $\bar{A} > 80$ km.

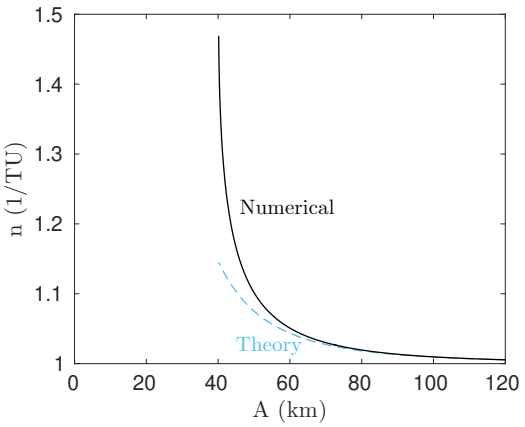

Figure 6: Comparison between the numerical value of n_{QSO} and its theoretical prediction $1+\dot{\bar{\alpha}}$. The time unit TU is equal to 1.288 hours.

In the validity regime of Eq. (20), the in-plane and out-of-plane components of motion can be decoupled and reduced to the linear systems

$$\begin{bmatrix} \dot{\bar{\delta}}_x \\ \dot{\bar{\delta}}_y \end{bmatrix} = \begin{bmatrix} 0 & D_x \\ D_y & 0 \end{bmatrix} \begin{bmatrix} \bar{\delta}_x \\ \bar{\delta}_y \end{bmatrix} - e \begin{bmatrix} d_x \sin\bar{\alpha} \\ d_y \cos\bar{\alpha} \end{bmatrix}, \tag{22}$$

$$\begin{bmatrix} \dot{\bar{K}}_5 \\ \dot{\bar{K}}_6 \end{bmatrix} = \begin{bmatrix} -\zeta \sin(2\,\bar{\alpha}) & -\epsilon + \zeta \cos(2\,\bar{\alpha}) \\ \epsilon + \zeta \cos(2\,\bar{\alpha}) & \zeta \sin(2\,\bar{\alpha}) \end{bmatrix} \begin{bmatrix} \bar{K}_5 \\ \bar{K}_6 \end{bmatrix}, \tag{23}$$

where

$$D_x = 2\left(\frac{\mathcal{K}-\mathcal{E}}{3\,\pi\,\bar{A}^3}\right) > 0, \tag{24a}$$

$$D_y = -\frac{3}{2} + 2\left(\frac{\mathcal{K}-4\,\mathcal{E}}{3\,\pi\,\bar{A}^3}\right) < 0, \tag{24b}$$

$$d_x = 2\left(\frac{\mathcal{K}-7\,\mathcal{E}}{9\,\pi\,\bar{A}^2}\right) < 0, \tag{24c}$$

$$d_y = \left(\frac{52\,\mathcal{E}-\mathcal{K}}{9\,\pi\,\bar{A}^2}\right) > 0, \tag{24d}$$

and

$$\zeta = \left(\frac{2\,\mathcal{K}-5\,\mathcal{E}}{6\,\pi\,\bar{A}^3}\right), \tag{25a}$$

$$\epsilon = \frac{\mathcal{E}}{2\,\pi\,\bar{A}^3}. \tag{25b}$$

The interested reader may find the analytical solution of these equations in Ref. [20]. Meanwhile, Figure 7 shows the behaviour of the mean orbit elements $\bar{\delta}_x$ and $\bar{\delta}_y$ obtained from the osculating orbit elements of Eq. (19) over 400 orbital periods of Phobos. Although the secular evolutions of $\bar{\delta}_x$ and $\bar{\delta}_y$ differ quite significantly from the osculating values, we find that the trajectory of the spacecraft does not drift away from the vicinity of Phobos' orbit. This shows that,

in the averaged system, trajectories are bounded even when $\bar{\delta}_x$ is not exactly zero. At the same time, we can also conclude that an appropriate transformation between osculating and mean orbit element is mandatory in order to adequately capture the secular evolution of spacecraft in mid-altitude 3D QSO orbits. The problem of finding accurate initial conditions for the averaged system is addressed in the next Section.

7 Near-identity Transformation

In order to provide a detailed mapping between mean and osculating orbit elements, different methods of perturbation theories can be considered (see for instance [21], [4], [22] and references therein). We introduce the inverse transformation $T : [0, 2\,\pi] \times \mathcal{M} \to \mathcal{M}$ such that the reconstructed osculating orbit elements

$$\hat{\mathbf{oe}} = \bar{\mathbf{oe}} + \epsilon\, T(\nu, \bar{\mathbf{oe}}) \tag{26}$$

satisfy

$$\dot{\hat{\mathbf{oe}}} = \epsilon\, \boldsymbol{g}(\nu, \hat{\mathbf{oe}}) + \mathcal{O}(\epsilon^2). \tag{27}$$

In Eq. (27), ϵ is a formal small parameter[1] that emphasizes the slow evolution of the mean orbit elements $\bar{\mathbf{oe}}$ with respect to the fast variable θ. Under this assumption, the System (20) may be rewritten in vectorial form as $\dot{\bar{\mathbf{oe}}} = \epsilon\, \bar{\boldsymbol{g}}(\bar{\mathbf{oe}})$. From Eq. (26), it follows that

$$\begin{aligned} \epsilon\, \boldsymbol{g}(\nu, \bar{\mathbf{oe}} + \epsilon\, T(\nu, \bar{\mathbf{oe}})) &= \epsilon\, \bar{\boldsymbol{g}}(\bar{\mathbf{oe}}) + \epsilon \left(\frac{\partial T}{\partial \nu} + \frac{\partial T}{\partial \bar{\mathbf{oe}}}\, \epsilon\, \bar{\boldsymbol{g}}(\bar{\mathbf{oe}}) \right), \\ \epsilon\, \boldsymbol{g}(\nu, \bar{\mathbf{oe}}) &= \epsilon \left(\bar{\boldsymbol{g}}(\bar{\mathbf{oe}}) + \frac{\partial T}{\partial \nu} \right), \end{aligned} \tag{28a}$$

[1] consider $\epsilon \simeq A^{-2}$ for practical purposes

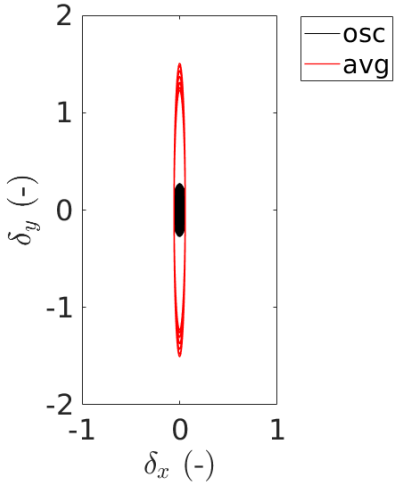

Figure 7: Evolution of the in-plane center of motion over 400 Phobos revolution with $\bar{\mathbf{oe}}(\nu_0) = \mathbf{oe}(\nu_0)$.

which implies

$$\frac{\partial T}{\partial \nu} \simeq \boldsymbol{g}(\nu, \bar{\boldsymbol{\alpha}}\mathbf{e}) - \bar{\boldsymbol{g}}(\bar{\boldsymbol{\alpha}}\mathbf{e}) \tag{29}$$

up to the first order in ϵ. Knowing that $\int_0^{2\,\pi} T(\nu, \bar{\boldsymbol{\alpha}}\mathbf{e})\,\mathrm{d}\nu = 0$, we then look for numerical approximations of T via the Fourier transformations outlined in [23]:

$$T(\nu, \bar{\boldsymbol{\alpha}}\mathbf{e}) = -i \sum_{i=1}^{N} \left(\frac{\boldsymbol{g}^{(k)}}{k} \right) \exp\left[-i\,k\,\nu\right]. \tag{30}$$

where $\boldsymbol{g}^{(k)}$ are the Fourier coefficients of $\boldsymbol{g}(\nu, \bar{\boldsymbol{\alpha}}\mathbf{e}) - \bar{\boldsymbol{g}}(\bar{\boldsymbol{\alpha}}\mathbf{e})$.

Based on this transformation, we calculate an approximate value of $\bar{\boldsymbol{\alpha}}\mathbf{e}$ and compare the numerical integration of (20) with Eqs. (22) and (23). The averaged initial conditions obtained from Eq. (19) are

$$\bar{\boldsymbol{\alpha}}\mathbf{e} = \begin{bmatrix} 4.21151847992516 \\ 0.613104203916773 \\ -0.00104870967949794 \\ -0.0793524699676065 \\ 0.296432612194867 \\ -0.179780157819618 \end{bmatrix} \tag{31}$$

and yields the plots of Fig. 8 and 9. We find that satellites in orbit around Phobos trace out prolate ellipses whose center oscillates in the δ_y direction. Meanwhile, K_5 and K_6 values follow a pulsating circle with time-varying radius $\bar{B}(\nu)$.

8 Nonlinear Lyapunov Controller

In this Section, we finally apply the near-identity transformation to derive a Lyapunov control law for the orbit maintenance of a satellite in a mid-altitude QSO orbit. Let $\bar{\boldsymbol{\alpha}}\mathbf{e}^*$ denote the "desired" mean relative orbit elements (i.e., the one obtained from the numerical integration of Eq. 1), whereas $\bar{\boldsymbol{\alpha}}\mathbf{e}$ are the "actual" mean relative orbit elements. The coordinates $\bar{\boldsymbol{\alpha}}\mathbf{e}$ differ from $\bar{\boldsymbol{\alpha}}\mathbf{e}^*$ because of injection errors such as $\begin{bmatrix} 109, & 111, & -86, & 7.74 \times 10^{-3}, & -0.12, & -0.11 \end{bmatrix}^T$ (m, m/s) that cause the actual trajectory to slowly drift away from the nominal one. Furthermore, assuming $\boldsymbol{u} \simeq \mathcal{O}(e) << 1$, Eq. (12) may be rewritten as

$$\dot{\boldsymbol{\alpha}}\mathbf{e} = \epsilon\,\boldsymbol{g}(\nu, \boldsymbol{\alpha}\mathbf{e}) + h(\nu, \boldsymbol{\alpha}\mathbf{e})\,\boldsymbol{u}, \tag{32}$$

where ϵ is the formal parameter of Section 7 and

$$h(\nu, \boldsymbol{\alpha}\mathbf{e}) = \begin{bmatrix} -\sin\theta & -2\,\cos\theta & 0 \\ -\left(\dfrac{\cos\theta}{A}\right) & 2\left(\dfrac{\sin\theta}{A}\right) & 0 \\ 0 & 2 & 0 \\ -2 & 0 & 0 \\ 0 & 0 & \cos\nu \\ 0 & 0 & -\sin\nu \end{bmatrix}. \tag{33}$$

We may also assume that $\boldsymbol{u}$ causes equivalent changes in both the osculating and mean relative orbit element domains such that

$$\dot{\bar{\boldsymbol{\alpha}}}\mathbf{e} = \epsilon\,\bar{\boldsymbol{g}}(\bar{\boldsymbol{\alpha}}\mathbf{e}) + h(\nu, \bar{\boldsymbol{\alpha}}\mathbf{e})\,\boldsymbol{u}. \tag{34}$$

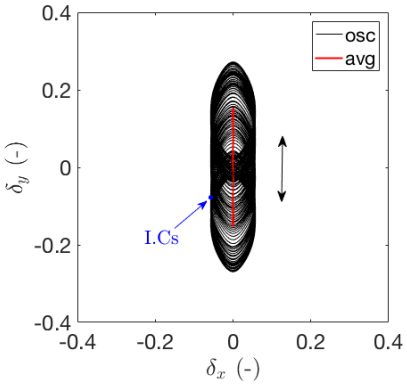

Figure 8: In-plane offset evolution over 100 Phobos orbits.

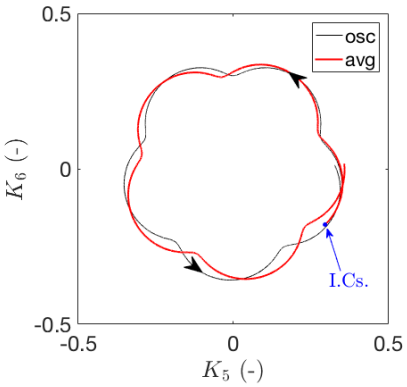

Figure 9: Out-of-plane motion over 400 Phobos orbits.

Here, we assume that $h(\nu, \mathbf{oe})$ can be computed using $\bar{\mathbf{oe}}$ rather then its osculating counterpart, which is adequate as long as we are willing to introduce an error of order ϵ.

Next, consider the equations of motion for the nominal mean relative orbit elements, i.e., $\dot{\bar{\mathbf{oe}}}^* = \epsilon\, \bar{\boldsymbol{g}}(\bar{\mathbf{oe}}^*)$, and define a positive definite Lyapunov control function with

$$V(\Delta\bar{\mathbf{oe}}) = \frac{1}{2}\, \Delta\bar{\mathbf{oe}}^T\, \Delta\bar{\mathbf{oe}}, \tag{35}$$

where $\Delta\bar{\mathbf{oe}} = \bar{\mathbf{oe}} - \bar{\mathbf{oe}}^*$. The first derivative of $V(\Delta\bar{\mathbf{oe}})$ then yields

$$\begin{aligned} \dot{V}(\Delta\bar{\mathbf{oe}}) &= \Delta\bar{\mathbf{oe}}^T\, \Delta\dot{\bar{\mathbf{oe}}}, \\ &= \Delta\bar{\mathbf{oe}}^T\, \{\epsilon\, [\bar{\boldsymbol{g}}(\bar{\mathbf{oe}}) - \bar{\boldsymbol{g}}(\bar{\mathbf{oe}}^*)] + h(\nu, \bar{\mathbf{oe}})\, \boldsymbol{u}\} \end{aligned} \tag{36}$$

and must be equal to $-\Delta\bar{\mathbf{oe}}^T\, P\, \Delta\bar{\mathbf{oe}}$, where P is a positive-semidefinite matrix, in order to ensure the stability of the nonlinear control law. Noting that $h(\nu, \bar{\mathbf{oe}})$ is a nonsquare matrix, Eq. (36) implies

$$\boldsymbol{u} = -(h^T\, h)^{-1}\, h^T\, \{\epsilon\, [\bar{\boldsymbol{g}}(\bar{\mathbf{oe}}) - \bar{\boldsymbol{g}}(\bar{\mathbf{oe}}^*)] + P\, \Delta\bar{\mathbf{oe}}\}\,, \tag{37}$$

which resembles the nonlinear Lyapunov controller disclosed in Ref. [24]. In fact, inspired by [24], we implement a time-varying gain matrix P so as to maximize the changes in A, α, K_5 and

K_6 when it is more appropriate. The gain matrix reads as

$$P = \text{diag}\left[P_A, \quad P_\alpha, \quad P_{\delta_x} \quad P_{\delta_y} \quad P_{K_5}, \quad P_{K_6}\right], \tag{38a}$$

$$P_A = 10^{-3} + 3\left(\frac{\sin\theta + 2\,\cos\theta}{2.2361}\right)^N, \tag{38b}$$

$$P_\alpha = 10^{-3} + 3\left(\frac{-\cos\theta + 2\,\sin\theta}{2.2361}\right)^N, \tag{38c}$$

$$P_{\delta_x} = 0.3, \tag{38d}$$

$$P_{\delta_y} = 0.3, \tag{38e}$$

$$P_{K_5} = 10^{-3} + 3\,(\cos\nu)^N, \tag{38f}$$

$$P_{K_6} = 10^{-3} + 3\,(\sin\nu)^N, \tag{38g}$$

where N is an even integer number (e.g., $N = 2$), and yields the controlled trajectory of Fig. 10. The controller is switched on as soon as the distance between the actual and nominal trajectory

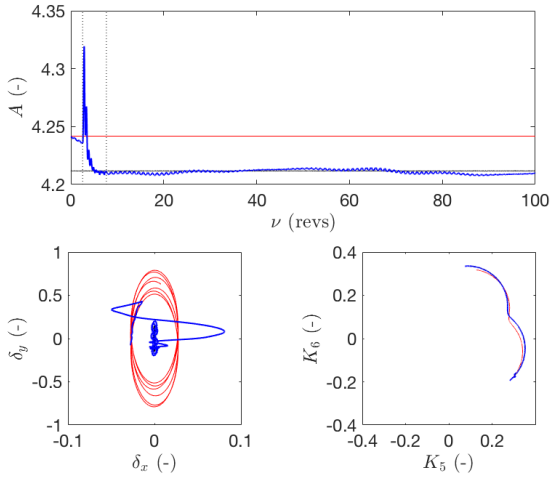

Figure 10: Controlled and Uncontrolled trajectories as seen in the relative orbit element space.

exceeds 10 km, affects the dynamical evolution of the spacecraft for several orbital revolutions around Phobos, and finally cutoff when the error is below 100 m. This control logic results in a long thrusting arc where $\|\boldsymbol{u}\|$ never exceeds the normalized value of 0.1 (Fig. 11), corresponding to approximately 0.11 mm/s^2. When integrated over the entire duration of the simulation, the control profile yields the total amount of ΔV produced, which is equal to 2.09 m/s.

The small quantity would be make the Lyapunov controller very attractive for in-situ operations. Unfortunately, the duration of the thrusting arc, along with the impossibility to implement autonomous control law onboard MMX, would make the practical implementation of the control law in Eq. (37) extremely challenging. Nevertheless, the value identified by this simulation could be useful for the design of the mission, as it provides mission designers with an order of magnitude for comparison with the actual control law that will be implemented on the spacecraft.

9 Conclusions

This paper presented a new set of equations of motion for mass-particles in the vicinity of Phobos. The equations are valid for mid-altitude quasi-planar retrograde orbits around the planetary satellite ($A > 80$ km) and accurately describe the long-term evolution of a spacecraft in this orbital regime. A near-identity transformation was applied in order to correctly transform from osculating to mean relative orbit elements and gain semi-analytical insight into the problem. This transformation enabled the derivation of a nonlinear Lyapunov control law based on mean relative orbit element differences. The controller was capable of nullifying injection errors and steer the spacecraft back to its nominal path regardless of the complexities generated by the eccentricity of the Martian moon and out-of-plane oscillations. Based on this result, quasi-QSO orbits seem to offer an interesting design option for spacecraft missions to Phobos and are advocated for close investigations of this small body.

References

[1] Y. Kawakatsu, K. Kuramoto, N. Ogawa, H. Ikeda, Y. Mimasu, G. Ono, H. Sawada, K. Yoshikawa, T. Imada, H. Otake, H. Kusano, K. Yamada, M. Otsuki, and M. Baba, "Mission concept of Martian Moons eXploration (MMX)," paper 40742 presented at the 68th International Astronautical Congress, Adelaide, Australia, 2017.

[2] S. Murchie, P. Thomas, A. Rivkin, and N. Chabot, "Phobos and Deimos," in *Asteroid IV*, pp. 451–467, University of Arizona Press, 2015.

[3] H. Ikeda, S. Mitani, Y. Mimasu, G. Ono, K. Nigo, and Y. Kawakatsu, "Orbital operations strategy in the vicinity of phobos," paper ISSFD-2017-008 presented at the International Symposium of Space Flight Dynamics in Matsuyama, Japan, 2017.

[4] M. Lara, "Nonlinear librations of distant retrograde orbits: a perturbative approach – the Hill problem case," *Nonlinear Dynamics*, 2018.

[5] A. I. Kogan, "Distant satellite orbits in the restricted circular three-body problem," *Cosmic Research (Translation of Kosmicheskie Issledovaniya)*, vol. 26, pp. 705–710, 1989.

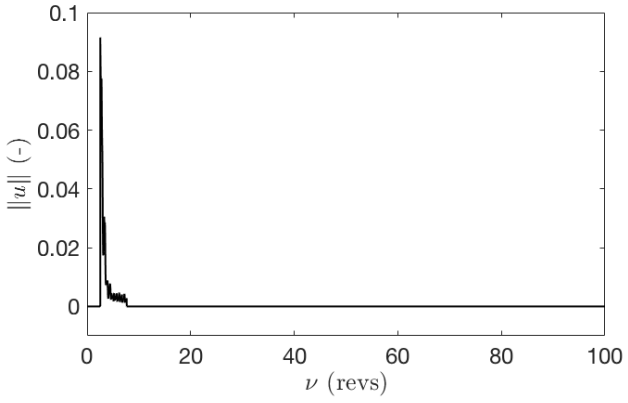

Figure 11: Control Profile generated by the Lyapunov nonlinear controller.

[6] K. Yamanaka and F. Ankersen, "New state transition matrix for relative motion on an arbitrary elliptical orbit," *Journal of Guidance, Control, and Dynamics*, vol. 25, pp. 60–66, jan-feb 2002.

[7] A. Farres and Á.. Jorba, "Orbital dynamics of a solar sail near L1 and L2 in the elliptic Hill problem," (Naples, Italy), paper IAC-12.C1.6.4 presented at the 63rd International Astronautical Congress, Naples, Italy, 2012.

[8] G. Voyatzis, I. Gkolias, and H. Varvoglis, "The dynamics of the elliptic Hill problem: Periodic orbits and stability regions," *Celestial Mechanics and Dynamical Astronomy*, vol. 113, no. 1, pp. 125–139, 2012.

[9] R. A. Broucke, "Stability of periodic orbits in the elliptic, restricted three-body problem," *AIAA Journal*, vol. 7, no. 6, pp. 1003–1009, 1969.

[10] D. J. Scheeres, S. Van wal, Z. P. Olikara, and N. Baresi, "The dynamical environment for the exploration of phobos," paper ISSFD-2017-007 presented at the 28th International Symposium on Space Flight Dynamics, Matsuyama, Japan, 2017.

[11] G. Gómez and J. Mondelo, "The dynamics around the collinear equilibrium points of the RTBP," *Physica D: Nonlinear Phenomena*, vol. 157, no. 4, pp. 283–321, 2001.

[12] Z. P. Olikara and D. J. Scheeres, "Numerical method for computing quasi-periodic orbits and their stability in the restricted three-body problem," paper AAS 12-361 presented at the 2012 AIAA/AAS Astrodynamics Specialist Conference, Minneapolis, MN, 2012.

[13] N. Baresi, Z. Olikara, and D. J. Scheeres, "Fully numerical methods for continuing families of quasi-periodic invariant tori in astrodynamics," *The Journal of the Astronautical Sciences*, vol. 65, no. 2, pp. 157–182, 2018.

[14] Z. P. Olikara, *Computation of Quasi-periodic Tori and Heteroclinic Connections in Astrodynamics using Collocation Techniques*. PhD thesis, University of Colorado Boulder, 2016.

[15] N. Baresi, *Spacecraft Formation Flight on Quasi-periodic Invariant Tori*. PhD thesis, University of Colorado Boulder, 2017.

[16] N. Baresi and D. J. Scheeres, "Quasi-periodic invariant tori of time-periodic dynamical systems: Applications to small body exploration," paper IAC-16.C1.7.4x32824 presented at the 67th International Astronautical Congress, Guadalajara, Mexico, 2016.

[17] A. J. Sinclair, R. E. Sherrill, and A. T. Lovell, "Geometric interpretation of the tschauner-hempel solutions for satellite relative motion," *Advances in Space Research*, vol. 55, no. 9, pp. 2268–2279, 2015.

[18] F. Cabral, "On the stability of quasi-satellite orbits in the Elliptic Restricted Three-Body Problem," Master's thesis, Universidade Técnica de Lisboa, 2011.

[19] M. Abramowitz, *Handbook of Mathematical Functions*. 1974.

[20] N. Baresi, L. Dell'Elce, J. Cardoso dos Santos, and Y. Kawakatsu, "On the long-term evolution of mid-altitude quasi-satellite orbits around phobos," *Nonlinear Dynamics*.

[21] M. Lara, J. Palacian, and R. P. Russell, "Mission design through averaging of perturbed Keplerian systems: the paradigm of an Enceladus orbiter," *Celestial Mechanics and Dynamical Astronomy*, vol. 108, pp. 1–22, 2010.

[22] J. Cardoso dos Santos, S. Ferrer, and D. J. Scheeres, "Study of the roto-translational motion using intermediaries: Numerical experiments," *Celestial Mechanics and Dynamical Astronomy, Submitted*, 2018.

[23] T. Ely, "Transforming mean and osculating elements using numerical methods," (Naples, Italy), paper AAS 10-139 presented at the 20th AAS/AIAA Space Flight Mechanics Meeting, San Diego, CA, 2010.

[24] H. Schaub, S. R. Vadali, J. L. Junkins, and K. T. Alfriend, "J2 invariant relative orbits for spacecraft formations," *Journal of the Astronautical Science*, vol. 48, no. 1, pp. 69–87, 2000.